Effects of Surface Depression on Pool Convection and Geometry in Stationary GTAW

Arc pressure at peak duration produces deep penetration in pulsed current gas tungsten arc welding

BY S. H. KO, S. K. CHOI AND C. D. YOO

ABSTRACT. The effects of surface depression on pool convection and geometry in stationary GTAW are simulated numerically under DC and pulsed-current conditions. Welding current and Marangoni flow affect surface depression and velocity such that inward flow by the current and positive surface-tension gradient acts to decrease surface depression. Arc pressure is found to be a major factor in surface depression and in fluctuations of free surface and flow velocity. While arc pressure at the low current range has negligible effects on surface depression and pool geometry, it should be considered in the high current range. Under the pulsed current condition, deep penetration is produced mainly by arc pressure at peak duration. The solid-liquid interface profile at the pool center and periphery becomes similar to that of peak and base current, respectively, and penetration is closely correlated to surface depression.

Introduction

Because weld pool convection was found to have significant effects on the bead width and penetration in arc welding (Ref. 1), extensive research has been undertaken to reveal the relationship between pool convection and geometry (Refs. 2–10). Among the various factors affecting pool convection, electromagnetic force and surface-tension gradient are the most important. Because the electromagnetic force generates circulation within the molten pool in a downward direction, penetration increases by pool convection. The rotating direction of Marangoni flow depends on the surface-tension gradient, which is affected by minor elements such as sulfur composition in the base metal. These convection patterns with heat input from the arc determine pool geometry.

S. H. KO and C. D. YOO are with the Department of Mechanical Engineering, KAIST, Taejon, Korea. S. K. CHOI is with the School of Mechanical Engineering, Kyungpook National Univ., Taegu, Korea.

Numerical methods have been employed to predict pool convection, and the calculated pool geometry was in agreement with the experimental result (Refs. 2, 5). One of the general assumptions made to simplify numerical computation is the molten pool surface is flat (Refs. 2–4). Another assumption of a deformed surface depression was employed (Refs. 6–8) using the surface profile in an equilibrium state by minimizing the potential energy (Ref. 9). Several attempts were made to include the free surface under the direct current (DC) condition (Refs. 10, 11). While three-dimensional pool geometry was calculated for nonautogenous welding using surface elevation, the effect of arc pressure was not considered (Ref. 10). A numerical model for a full penetration weld with two free surfaces was presented (Ref. 11). Because the focus was the Marangoni effect on a free surface, the effect of the electromagnetic force was ignored and the pool had a cylindrical shape. Therefore, dynamic effects of surface depression on pool convection and its geometry have not been fully understood under DC and pulsed-current conditions.

In this work, dynamic variations of surface depression and pool convection in DC and pulsed-current gas tungsten arc welding (GTAW) are calculated numerically by employing the Volume of Fluid (VOF) method (Ref. 12). The solid-liquid interface of a molten pool is computed by solving the energy equation, and the effects of arc pressure, current and surface-tension gradient on surface depression and convection are analyzed based on the calculated results. Causes of deep penetration by the pulsed current are also simulated.

KEY WORDS

Surface Depression
Pool Convection
GTAW
Direct Current
Pulsed Current
Marangoni Flow
Volume of Fluid Method

Formulation

Since the effects of a free surface are emphasized in this work, the following assumptions are made in the formulation: 1) fluid flow in the axisymmetric molten pool is incompressible and laminar, 2) the effect of the drag force from the plasma jet is neglected, and 3) material properties are constant. The principle of the VOF method for calculating fluid flow with a free surface is described briefly because it was explained in detail in other works (Refs. 8, 12, 13). The solution domain is divided by the staggered grid and the function F is defined to describe the fluid volume ratio within the cell. The governing equations consist of the continuity, momentum equations and an additional equation relating to the function F as follows:

$$\nabla \cdot \vec{v} = 0 \tag{1}$$

$$\frac{\partial \vec{v}}{\partial t} + (\vec{v} \cdot \nabla)\vec{v} = -\frac{1}{\rho} \nabla P + \nu \nabla^2 \vec{v} + \frac{1}{\rho} \vec{J} \times \vec{B} + \vec{g}\beta(T - T_{liq}) \tag{2}$$

$$\frac{\partial F}{\partial t} + (\vec{v} \cdot \nabla)F = 0 \tag{3}$$

where $\vec{v}$ represents the velocity vector, P the pressure, ρ the mass density, ν the viscosity, $\vec{J}$ the current density, $\vec{B}$ the magnetic flux, β the thermal expansion and T_{liq} the melting temperature. The electromagnetic and buoyancy forces in Equation 2 are included as the body force.

The energy equation is solved in an implicit manner to calculate the temperature and solid-liquid interface as follows:

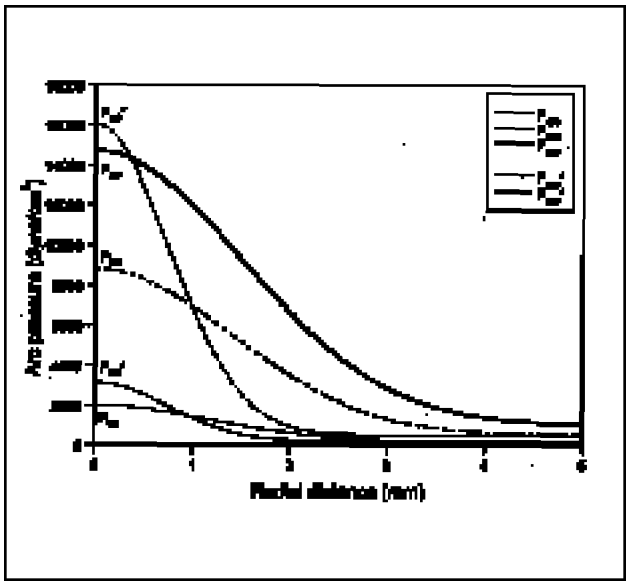

Fig. 1 — Arc pressure distributions on the pool surface.

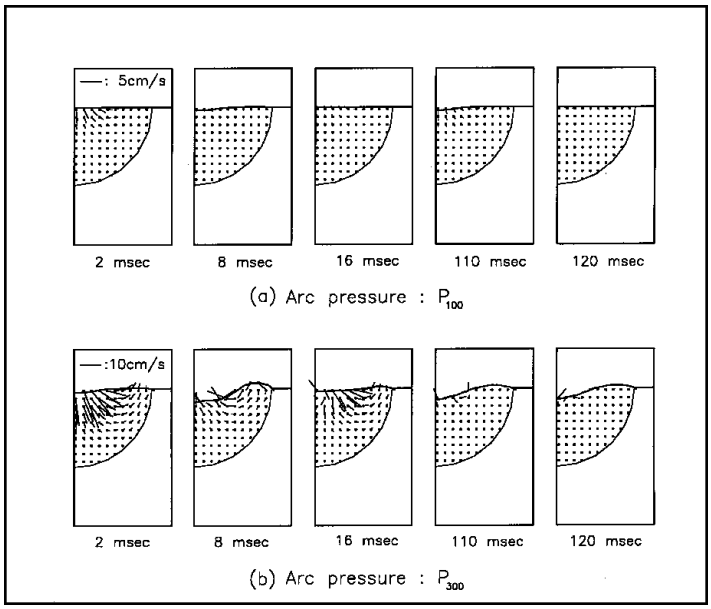

Fig. 2 — Surface depression and flow patterns for P_{100} and P_{300}. (I = 0A, γ = 1200 dyne/cm).

Table 1 — Material Properties of Mild Steel Used for Calculation

Mass Density, ρ	7860 (kg/m³)
Kinematic Viscosity, ν	5.6 x 10⁻⁷ (m²/s)
Surface Tension Coefficient, γ	1200 (dyne/cm)
Surface Tension Gradient, dγ/dT	±4.9 x 10⁻⁴ (N/mK)
Electrical Conductivity, σ_e	8.54 x 10⁵ (mho/m)
Permeability, μ_o	4π x 10⁻⁷ (H/m)
Thermal Conductivity, k	30 (W/mK)
Specific Heat, C_p	795 (J/kgK)
Latent Heat of Fusion, ΔH	272 (kJ/kg)
Liquidus Temperature, T_{liq}	1809 (K)
Solidus Temperature, T_{sol}	1789 (K)
Distribution Parameter of Current Density, σ_j	3 (mm)
Distribution Parameter of Heat Flux, σ_q	3 (mm)

$$\rho C_p\left(\frac{\partial T}{\partial t}+v\cdot\nabla T\right)=\nabla\cdot(k\nabla T)+\dot{q}_j \qquad (4)$$

where C_p represents the specific heat, k the thermal conductivity and q_j the joule heating per unit volume. The latent heat, ΔH, is considered by increasing the specific heat in the temperature range of phase change as follows:

$$C_p^* = \frac{\Delta H}{(T_{liq}-T_{sol})} + C_p, \quad T_{sol} < T < T_{liq} \qquad (5)$$

As for the boundary conditions, the free-slip and no-slip conditions are imposed along the z-axis and on the solid-liquid interface, respectively. The arc pressure of a Gaussian distribution is exerted on the pool surface as shown in Fig. 1, where P_{100}, P_{200} and P_{300} represent arc pressure at welding current 100, 200 and 300 A (Ref. 11). To compare the effect of arc pressure distribution, modified pressures of P_{100}* and P_{200}* are introduced that have the same total arc forces of P_{100} and P_{200}, respectively. The heat flux and current density from the arc are also described using the Gaussian distribution on the free surface as follows:

$$q(r)=\frac{Q}{2\pi\sigma_q^2}\exp\left(-\frac{r^2}{2\sigma_q^2}\right)$$

$$\text{and } J(r)=\frac{I}{2\pi\sigma_j^2}\exp\left(-\frac{r^2}{2\sigma_j^2}\right) \qquad (6)$$

where σ_q and σ_j denote distribution parameters of heat flux and current density, respectively. Although the distributions of heat flux and current density may vary with surface depression, they are assumed to be constant because these distributions are not known. Marangoni flow due to the surface-tension gradient, (∂γ/∂T), is considered by imposing shear stress on the free surface as follows:

$$\tau=\left(\frac{\partial\gamma}{\partial T}\right)\left(\frac{\partial T}{\partial\psi}\right) \qquad (7)$$

where γ and ψ denote the surface-tension coefficient and tangential direction of the free surface, respectively. The SOLA-VOF code written in FORTRAN is modified to include the effects of electromagnetic force and surface-tension gradient.

Results and Discussions

Effects of Welding Parameters under the DC Condition

In order to investigate the effects of the process parameters on surface depression and pool convection, the molten pool is assumed to be a hemispherical shape having a radius of 5 mm without solving the energy equation. Physical properties corresponding to those of mild steel are listed in Table 1 (Refs. 14,15). Initial flow velocity within the molten pool is set to zero. When the pressures of P_{100} and P_{300} are exerted on the surface without the current and surface-tension gradient, the calculated free surface profile and flow pattern are like that illustrated in Fig. 2. Small surface depressions and flow velocity are developed at P_{100}, and they continue to fluctuate until the steady state is reached, which represents

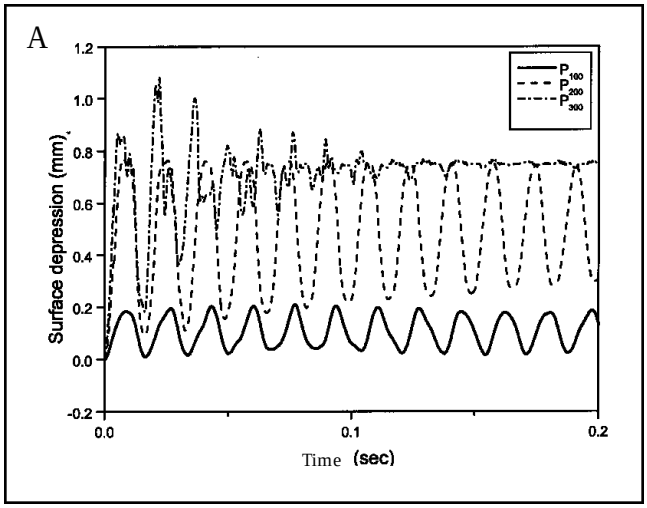

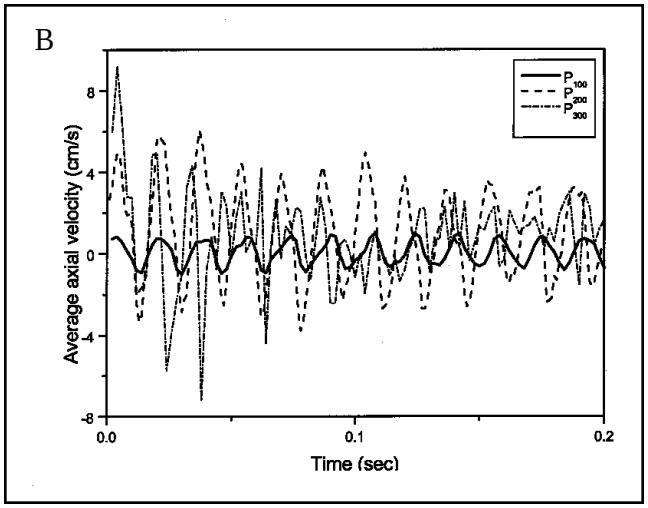

Fig. 3 — Effects of arc pressure on surface depression and axial velocity (I = 0A, γ = 1200 dyne/cm). A — Surface depression; B — average axial velocity.

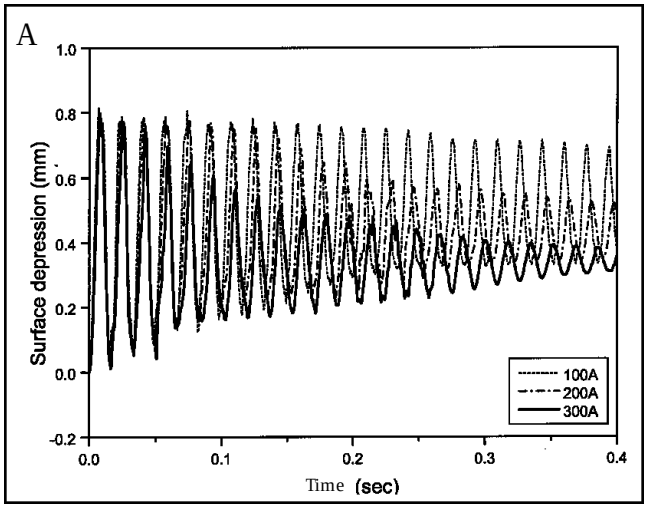

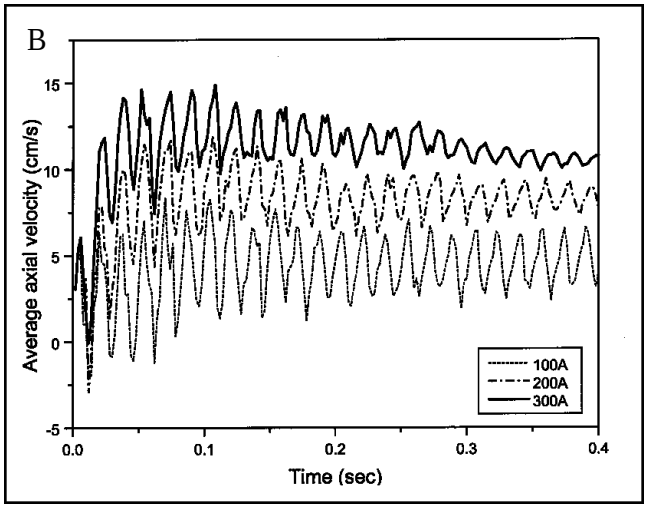

Fig. 4 — Effects of current on surface depression and axial velocity (P = P_{200}, γ = 1200 dyne/cm). A — Surface depression; B — average axial velocity.

weld pool oscillation (Ref. 16). With a higher arc pressure of P_{300}, surface depression increases and faster flow velocity is induced.

Variations of surface depression at the surface center and average axial velocity along the z-axis are shown in Fig. 3. As expected, surface depression increases for higher arc pressure. While free surface and flow velocity vibrate periodically for P_{100} and P_{200}, the amplitude of P_{300} decays rapidly with the lapse of time because high arc pressure acts as a restraint force on surface fluctuation. Since the free surface and axial velocity vibrate at the same frequency, velocity fluctuation is induced by arc pressure.

With the arc pressure fixed to P_{200}, the effect of current on surface depression and axial velocity is shown in Fig. 4. For the low current of 100 A, surface depression is not affected and is almost similar to the case of 0A in Fig. 3A. When the current increases, surface depression and the amplitude of surface fluctuation decrease. The reason is explained using axial velocity in Fig. 4B. As the electromagnetic force increases with higher current, fast inward flow on the pool surface fills the depressed pool center, which reduces the surface depression and its fluctuation.

To identify the causes of free surface and flow velocity fluctuation, comparisons are made for the cases with P_{200} and without arc pressure (*i.e.*, P = 0) as shown in Fig. 5. Without arc pressure, the free surface at the pool center rises slightly to 0.1 mm because of the inward flow and the amplitude of surface fluctuation is quite small. When arc pressure of P_{200} is imposed, surface depression and its amplitude increase significantly. Flow velocity also fluctuates with large amplitude as shown in Fig. 5B, but its magnitude becomes smaller than that of P = 0. It clearly indicates arc pressure is responsible for surface depression and fluctuations of free surface and flow velocity, while current affects flow velocity and decaying of fluctuation.

The effects of surface tension are illustrated in Fig. 6 where the surface-tension coefficients of 1200 and 1800 dyne/cm, fixed arc pressure and current of P_{200} and 200 A are used for calculation. In this case, the effect of surface-

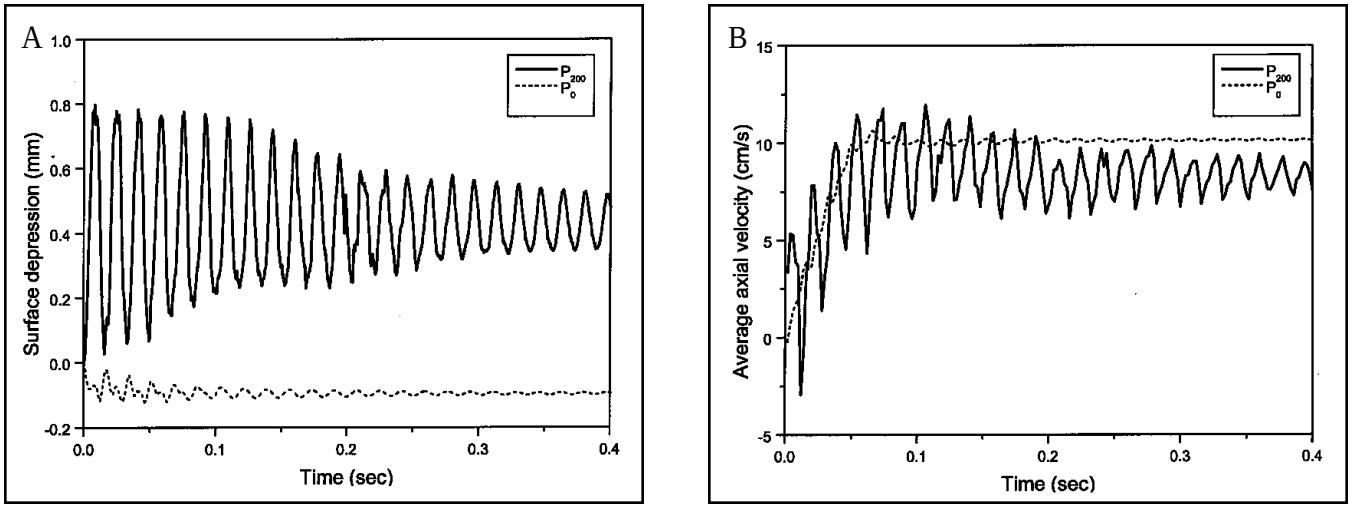

Fig. 5 — Comparison with and without effects of arc pressure (I = 200 A, γ = 1200 dyne/cm). A — Surface depression; B — average axial velocity.

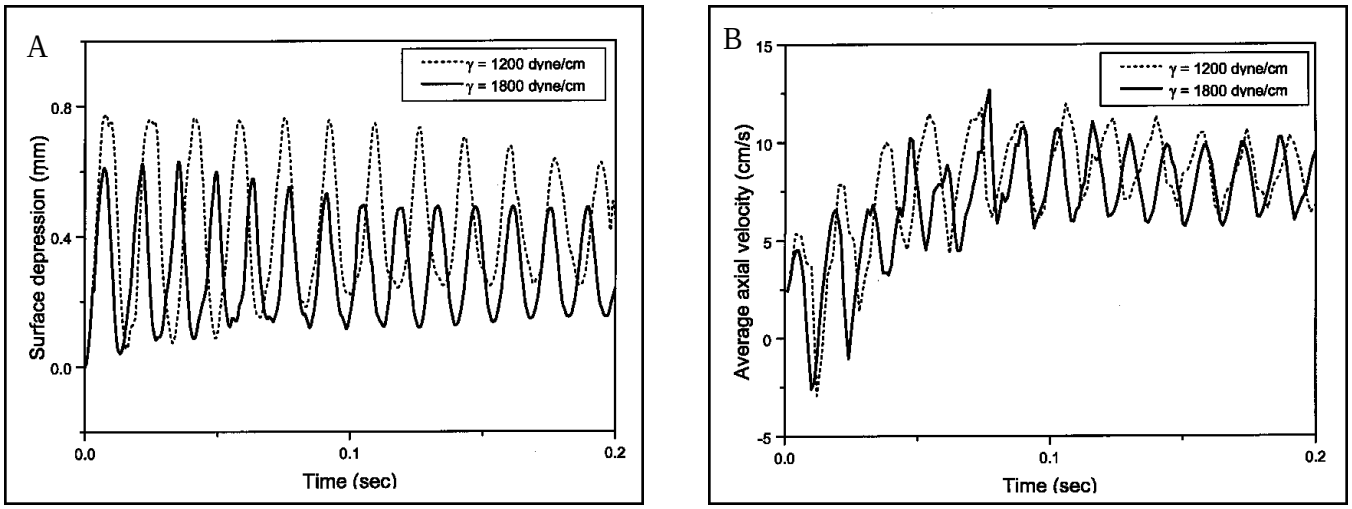

Fig. 6 — Effects of surface tension on surface depression and axial velocity (P = P_{200}, I = 200 A. A — Surface depression; B — average axial velocity.

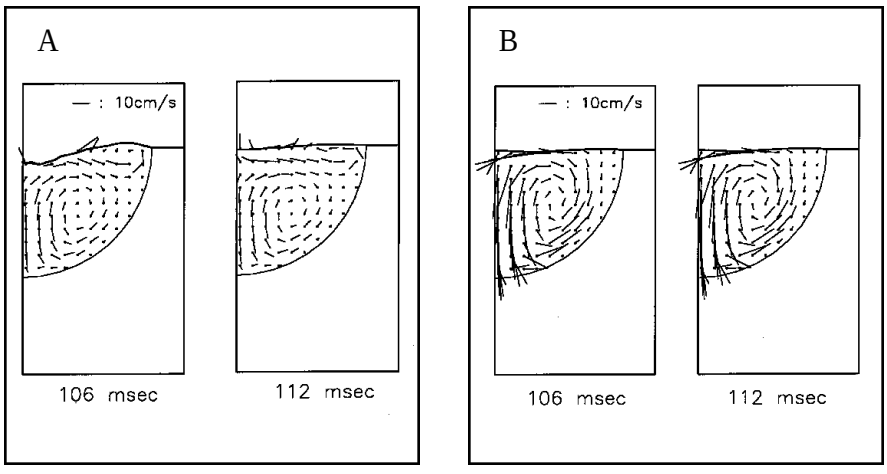

Fig. 7 — Surface profiles and convection patterns due to surface-tension gradient (P = P_{200}, I = 200 A). A — dγ/dT = –0.49 dyne/cmK; B — dγ/dT = 0.49 dyne/cmK.

tension gradient is ignored. Surface depression decreases with higher surface tension coefficient as in Fig. 6A because higher pressure is required to deform the pool surface of higher surface tension. However, the axial velocity is not affected by the surface tension coefficient as in Fig. 6B.

When the surface-tension gradients of ± .49 dyne/cmK are used with fixed pressure of P_{200} and current of 200 A, the surface profile and flow pattern are illustrated in Fig. 7. In the case of the negative surface-tension gradient, a double loop circulation is calculated as in Fig. 7A. When the surface-tension gradient is changed to the positive value, Marangoni and electromagnetic flow rotate in the same inward direction, which results in faster axial velocity. These flow patterns are similar to those of previous works

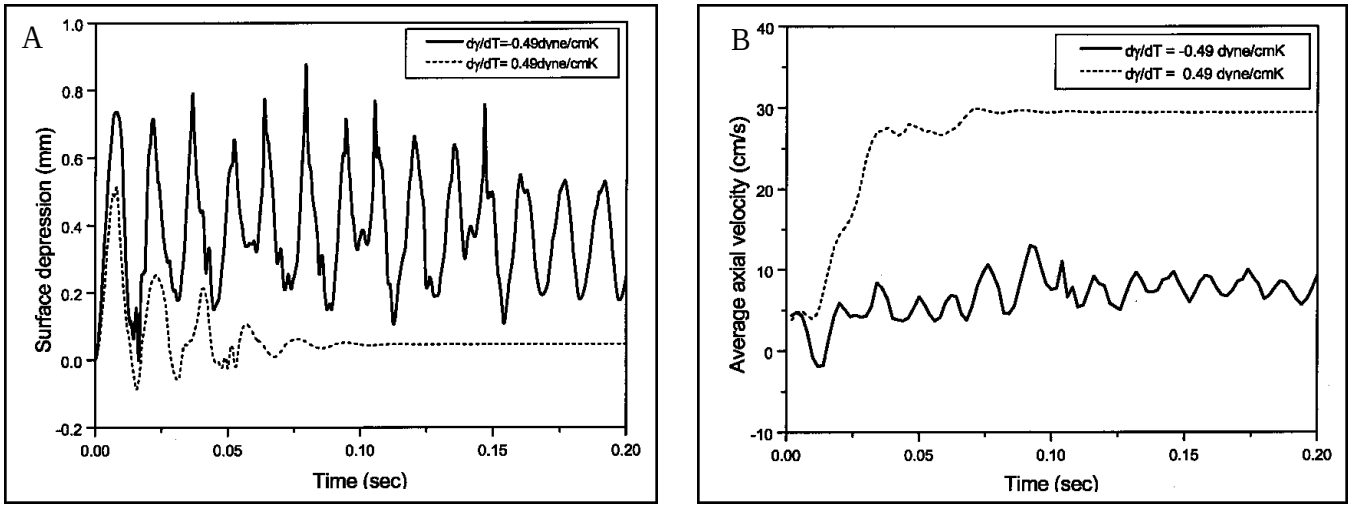

Fig. 8 — Effects of surface-tension gradient on surface depression and convection (P = P_{200}, I = 200 A). A — Surface depression; B — average axial velocity.

(Refs. 1–10). Variations of surface depression and axial velocity are shown in Fig. 8. With the negative surface-tension gradient, the pool surface continues to oscillate periodically as in Fig. 8A. Average axial velocity is small because the double loop circulation cancels the axial velocity components along the z-axis. With the positive surface-tension gradient, surface fluctuation decays rapidly and surface depression becomes almost negligible after 0.1 s. This phenomenon by the surface-tension gradient is more pronounced than that by the current in Fig. 5A because the inward flow velocity on the surface becomes much faster than that by the current in Fig. 5B. Therefore, the depressed pool center is filled by the inward flow at a much faster rate.

The calculated results of the flow pattern and solid-liquid interface in the steady state are illustrated in Fig. 9 where the surface-tension gradient of –0.49 dyne/cmK and current of 100 A are used. Comparing the results with P_{100} and without arc pressure (*i.e.*, P = 0), there is almost no difference in pool geometry because surface depression due to arc pressure is very small. When current and arc pressure are increased to 200 A and P_{200}, surface depression and the resultant penetration increase substantially, as shown in Fig. 10A. Without arc pressure as in Fig. 10B, the effects of surface depression become negligible, and penetration becomes shallow. Therefore, assumptions of the flat surface and surface depression in a steady state may not be valid in the high current range where the arc pressure and resultant surface depression have significant effects on pool geometry.

The effects of arc pressure distribution are illustrated in Fig. 11 where P_{100}* and P_{200}* in Fig. 1 are used for computation.

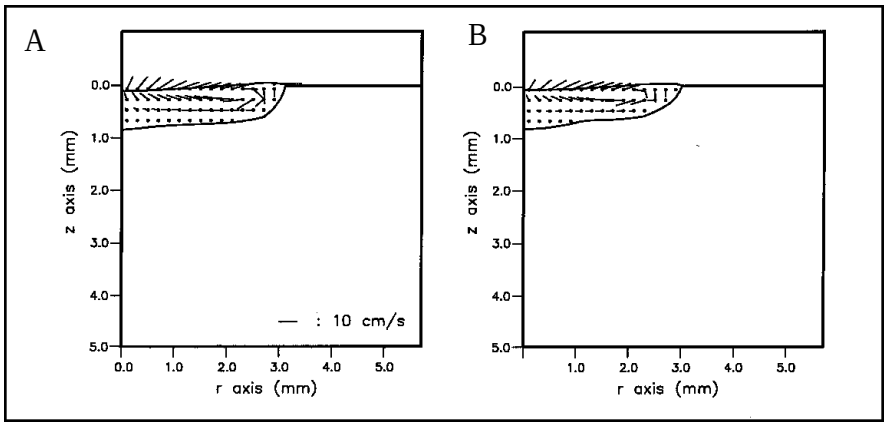

Fig. 9 — Flow pattern and solid-liquid interface at low current of 100 A (dγ/dT = –0.49 dyne/cmK). A — P = P_{100}; B — P = 0.

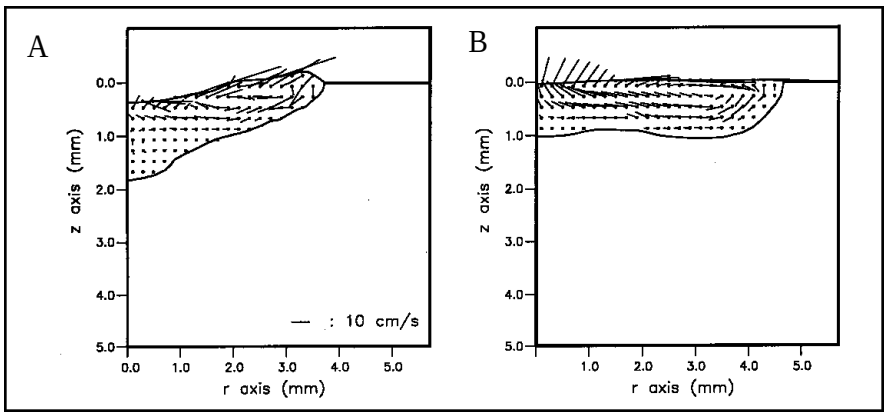

Fig. 10 — Flow pattern and solid-liquid interface at 200 A (dγ/dT = –0.49 dyne/cmK). A — P = P_{200}; B — P = 0.

In the case of P_{100}*, surface depression and penetration are similar to those of P_{100} in Fig. 9A because of low arc pressure. When arc pressure is increased to P_{200}*, deep penetration and narrow pool radius are calculated. Therefore, if the arc pressure distribution changes in the high current range due to arc length variation or other disturbances, the pool geometry is also influenced.

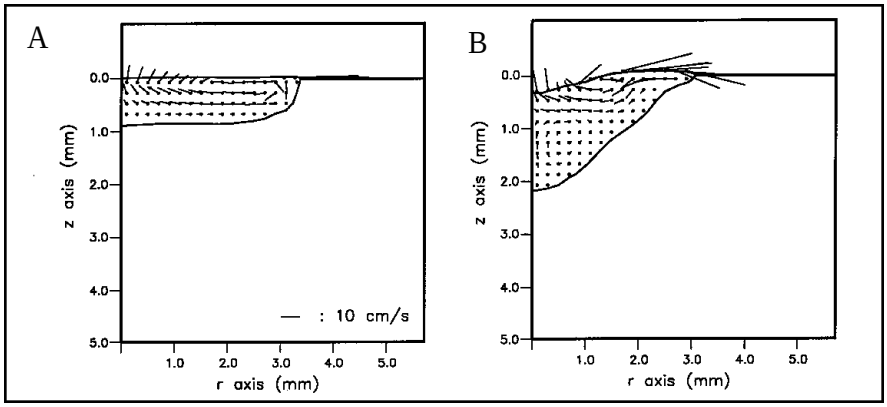

Fig. 11 — Flow pattern and solid-liquid interface for modified arc pressure distributions (dγ/dT = –0.49 dyne/cmK). A — P = P_{100}; B — P = P_{200}*.*

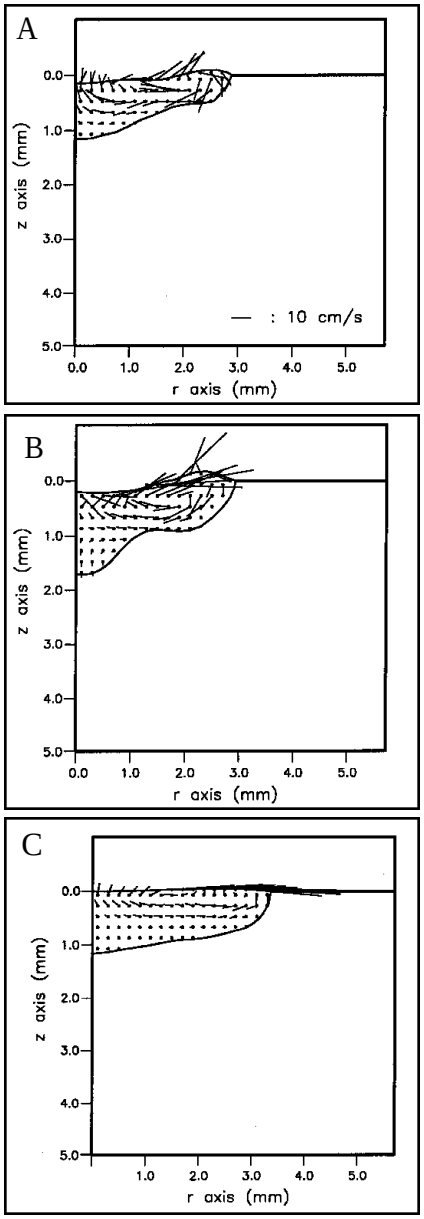

Fig. 12 — Flow pattern and solid-liquid interface for pulse current (I_p = 200 A, I_b = 100 A, dγ/dT = –0.49 dyne/cmK). A — f_p = 5 Hz, T_p = 10 ms; B — f_p = 10 Hz, T_p = 20 ms; C — f_p = 20 Hz, T_p = 10 ms.

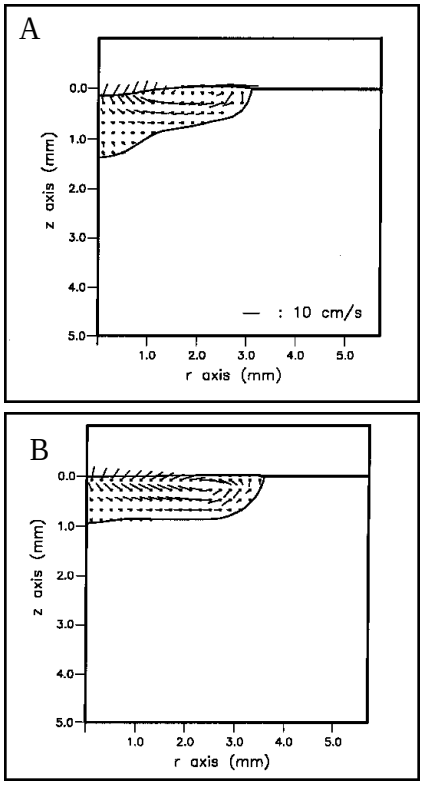

Fig. 13 — Effects of arc pressure and heat flux pulsing on solid-liquid interface (I_p = 200 A, I_b = 100 A, f_p = 10 Hz, T_p = 20 ms, dγ/dT = –0.49 dyne/cmK). A — Only arc pressure pulsing; B — only heat flux pulsing.

Effects of Pulsed Current

The effects of pulsed current on pool geometry are illustrated in Fig. 12 where the surface-tension gradient of –0.49 dyne/cmK, the base and peak currents of 100 and 200 A, and corresponding arc pressure of P_{100} and P_{200} are used for calculation. When the pulsing frequency is 5 Hz and peak duration is 10 ms (average current of 105 A), the penetration in Fig. 12A becomes deeper than that of DC 100 A in Fig. 9A. When the pulsing frequency and peak duration increase to 10 Hz and 20 ms (average current of 120 A), penetration in Fig. 12B becomes more pronounced and is almost equal to that of DC 200 A in Fig. 10A. The pool radius and penetration at the outer radius are almost the same as that of DC 100 A so the pool geometry becomes similar to a finger shape. When the peak duration of 10 ms and pulsing frequency of 20 Hz are used (Fig. 12C), penetration does not increase to that in Fig. 12B though the average current of 120 A is the same for both cases. It implies that the peak duration is an important factor in determining penetration, and sufficiently long peak duration is needed to provide enough momentum within the molten pool.

To find out the causes of deep penetration under the current pulsing condition of Fig.12B, two cases of pulsing of arc pressure and heat flux are simulated as shown in Fig. 13. The condition of pulsing arc pressure and constant heat flux generates deep penetration similar to a finger shape as shown in Fig. 13A. However, another condition of pulsing heat flux and constant arc pressure becomes similar to that of DC 100 A as in Fig. 13B. These results clearly show deep penetration is produced mainly by pulsing of arc pressure at peak duration rather than by pulsing of heat flux.

The relationship between surface depression and penetration is illustrated in Fig. 14 where pulsing frequency and peak time are 10 Hz and 20 ms, respectively. In this case, arc pressures of P_{100}* and P_{200}* are used for calculation. A close correlation between surface depression and penetration is observed such that the free surface is depressed just after current pulsing and penetration increases rapidly. After peak current, penetration decreases gradually. Peaks of surface depression and penetration coincide up to 0.5 s, because axial momentum by surface depression is delivered immediately in the small weld pool. When the pool size becomes larger after 0.5 s, there is a time delay between the maximum surface depression and penetration because it takes time to deliver axial momentum and heat by convection in the larger molten pool. The experimental verification and effects of temperature-dependent material properties need to be considered in future work.

Conclusions

Surface depression and pool geometry of DC and pulsed-current arc welding are calculated numerically, and the results lead to the following conclusions:

1) The free surface of a molten pool is depressed mainly by arc pressure, and in-

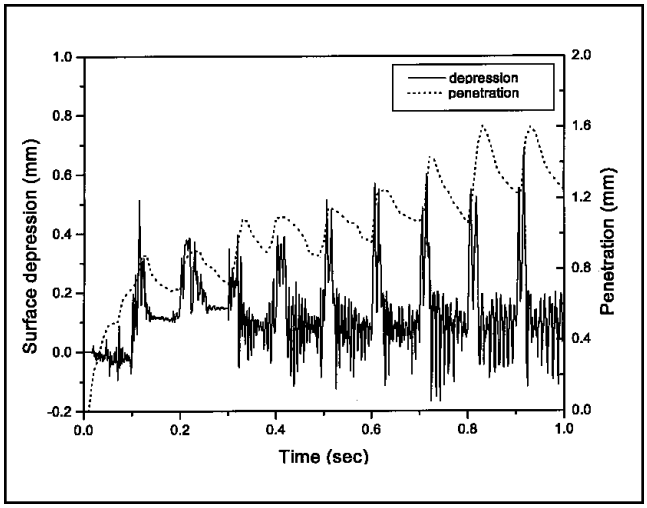

Fig. 14 — Relation between surface depression and penetration using P_{100} and P_{200}* (I_p = 200 A, I_b = 100 A, f_p = 10 Hz, T_p = 20 ms, $d\gamma/dT$ = –0.49 dyne/cmK).*

ward circulation by the current and Marangoni flow decreases surface depression and its fluctuation.

2) While arc pressure in the low current range has negligible effects on surface depression and pool geometry, the effects of arc pressure and surface depression should be considered in the high current range above 200 A.

3) Deep penetration in pulsed current welding is produced mainly by arc pressure at peak duration, and sufficiently long peak duration is needed for deep penetration.

Acknowledgments

The authors appreciate the financial support of the POSCO Research Institute and BK-21 project.

References

1. Heiple, C. R., and Roper, J. R. 1982. Mechanism for minor element effect on GTA fusion zone geometry. *Welding Journal* 61(4): 97-s to 102-s.

2. Kou, S., and Wang, Y. H. 1986. Weld pool convection and its effect. *Welding Journal* 65(3): 63-s to 70-s.

3. Oreper, G. M., Eagar, T. W., and Szekely, J. 1983. Convection in arc weld pools. *Welding Journal* 62(11): 307-s to 312-s.

4. Zacharia, T., David, S. A., Vitek, J. M., and Debroy, T. 1989. Weld pool development during GTA and laser beam welding of type 304 stainless steel, part I — theoretical analysis. *Welding Journal* 68(12): 499-s to 509-s.

5. Zacharia, T., David, S. A., Vitek, J. M., and Debroy, T. 1989. Weld pool development during GTA and laser beam welding of type 304 stainless steel, part II — experimental correlation. *Welding Journal* 68(12): 510-s to 519-s.

6. Tsai, M. C., and Kou, S. 1990. Electromagnetic-force-induced convection in weld pools with a free surface. *Welding Journal* 69(6): 241-s to 246-s.

7. Kim, S. D., and Na, S.-J. 1992. Effect of weld pool deformation on weld penetration in stationary gas tungsten arc welding. *Welding Journal* 71(5): 179-s to 193-s.

8. Choo, R. T. C., Szekely, J., and Westhoff, R. C. 1990. Modeling of high-current arcs with emphasis on free surface phenomena in the weld pool. *Welding Journal* 69(9): 346-s to 361-s.

9. Lin, M. L., and Eagar, T. W. 1985. Influence of arc pressure on weld pool geometry. *Welding Journal* 64(6): 163-s to 169-s.

10. Zacharia, T., Eraslan, A. H., and Aidun, D. K. 1988. Modeling of nonautogenous welding. *Welding Journal* 67(1): 18-s to 27-s.

11. Chen, Y., David, S. A., Zacharia, T., and Cremers, C. J. 1998. Marangoni convection with two free surfaces. *Numerical Heat Transfer*, Part A 33: 599–620.

12. Hirt, C. W., and Nichols, B. D. 1981. Volume of fluid (VOF) method for the dynamics of free boundaries. *Journal of Computational Physics* 39: 201–225.

13. Choi, S. K., Ko, S. H., Yoo, C. D., and Kim, Y. S. 1998. Dynamic simulation of metal transfer in GMAW — part 2: short-circuit transfer modes. *Welding Journal* 77(1): 45-s to 51-s.

14. Choo, R. T. C., and Szekely, J. 1991. The effect of gas shear stress on Marangoni flows in arc welding. *Welding Journal* 70(9): 223-s to 233-s.

15. Brandes, E. A., and Brook, G. B. 1992. *Smithells Metals Reference Book*, 7th Ed., Butterworth-Heinemann Ltd.

16. Renwick, R. J., and Richardson R. W. 1983. Experimental investigation of GTA weld pool oscillations. *Welding Journal* 62(2): 29-s to 35-s.

Correction

Figure 8 as it appears on page 353-s in "A Martensite Boundary on the WRC-1992 Diagram — Part 2: The Effect of Manganese," by D. J. Kotecki, published December 2000, is a duplicate of Fig. 7. The correct Fig. 8 appears below. The editors regret this error.

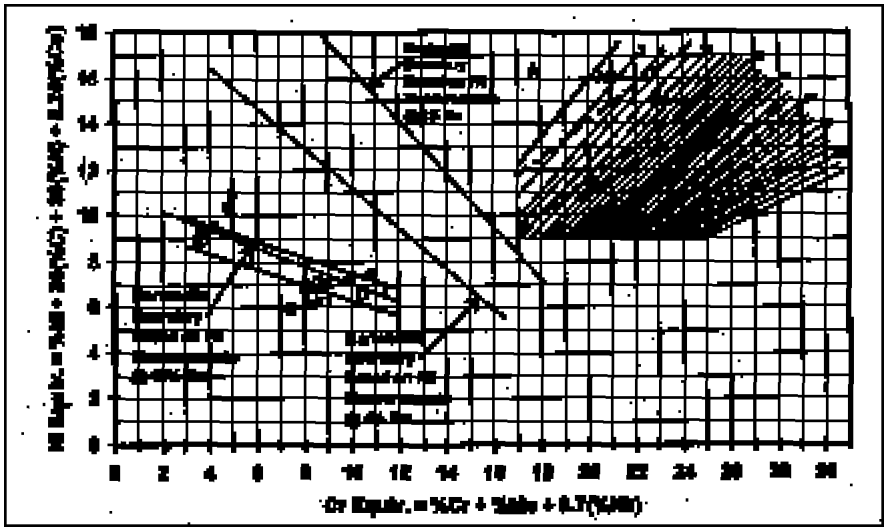

Bend/break results at 10% Mn on the WRC-1992 Diagram. Compositions that passed the 2T bend test are shown in solid circles. Compositions that cracked during bending are shown as open squares. Between the two parallel heavy lines, some compositions bent and some cracked. Above and to the right of the heavy lines, all compositions bent. Below and to the left of the heavy lines, all compositions cracked in bending